Construction and Building Materials 267 (2021) 121164

Contents lists available at ScienceDirect

Construction and Building Materials

journal homepage: www.elsevier.com/locate/conbuildmat

Relation between water permeability and chloride diffusivity of concrete under compressive stress: Experimental investigation and mesoscale lattice modelling

T.T. Tran [a], D.T. Pham [b], M.N. Vu [c,d,*], V.Q. Truong [a], X.B. Ho [a], N.L. Tran [e], T. Nguyen-Sy [f], Q.D. To [f]

[a] Departement of Civil Engineering, University of Transport and Communications, Viet Nam
[b] Departement of Civil Engineering, Hanoi University of Mining and Geology, Hanoi, Viet Nam
[c] Division of Construction Computation, Institute for Computational Science, Ton Duc Thang University, Ho Chi Minh City, Viet Nam
[d] Faculty of Civil Engineering, Ton Duc Thang University, Ho Chi Minh City, Viet Nam
[e] Faculty of Civil Engineering, Vinh University, Nghe An, Viet Nam
[f] Institute of Research and Development, Duy Tan University, Danang, Viet Nam

HIGHLIGHTS

- Transport properties of concretes under compressive stress are investigated.
- Water permeability is measured by tests on hollow cylindrical specimens.
- Bespoke test setup is used to measure the rapid chloride permeability.
- Hydro-damage lattice model is proposed to assess stress induced changes in transport properties.
- Relation between water permeability and chloride diffusivity is proposed.

ARTICLE INFO

Article history:
Received 21 June 2020
Received in revised form 22 September 2020
Accepted 29 September 2020
Available online 21 October 2020

Keywords:
Water permeability
Chloride diffusivity
Compressive stress
Concrete
Mesoscale
Hydro-mechanical lattice model

ABSTRACT

This paper presents experimental investigations and a lattice modelling of the water permeability and chloride diffusivity of concrete under compressive stress and then proposes relationships between these two transport properties. Two representative ordinary concretes usually used in structures, subjected to compressive loading and water seepage or chloride contact, are considered.

Water permeability tests were performed on hollow cylindrical samples in which the water diffuses in the radial direction through the sample thickness from the outer to inner surfaces under three different pressure gradients 3, 4 and 5 atm. Four compressive stresses (20%; 40%; 60% and 80% of the compressive strength) were applied on the sample top surface during the water permeability measurement. Rapid Chloride Permeability Testing (RCPT) is used to evaluate the chloride diffusivity. RCPT was carried out on cylindrical cores under four different stress levels (0; 25%; 50% and 75% of the stress at ultimate load).

Mesoscale hydro-mechanical lattice modelling is proposed to model the fluid flow and chloride ingress in concrete under stress. In such a model, concrete includes three constituents: cement, aggregates and interfacial transition zone (ITZ). A softening damage model is employed to describe the behaviour of the cement matrix and the ITZ, while the aggregates are assumed to be elastic. Hydro-mechanical parameters of concrete components are calibrated from the experimental results of both water permeability and chloride diffusion tests. The proposed model allows extrapolating the experimental results for higher compressive stress. A relation between water permeability and diffusivity coefficients is resulted from both experimental and numerical investigations for a large range of compressive stress.

1. Introduction

Water permeability and chloride diffusivity are two key parameters for assessing the serviceability and long-term durability of reinforced concrete (RC) structure exposed to aggressive environments. These transport properties depend on two main factors:

* Corresponding author at: Ton Duc Thang University, Ho Chi Minh City, Viet Nam.
E-mail address: vuminhngoc@tdtu.edu.vn (M.N. Vu).

https://doi.org/10.1016/j.conbuildmat.2020.121164
0950-0618/

interconnected porosity of mortar and micro-cracks in concrete. The latter one is controlled by the stress level and the stress path, while the porosity and its interconnectivity is essentially influenced by the ratio water/cement (w/c) as well as the compaction and the hydration degrees. Water permeability and chloride diffusion coefficients are usually individually evaluated by experimental or/and numerical investigations. Permeability of a porous medium is fluid flux through a unit area section under a unit pressure gradient. The permeability measurement methods of a concrete sample are divided into two categories: indirect and direct methods [55]. Main existing methods of the water permeability measure for concrete material has been recently reviewed and discussed by Amriou and Bencheikh [5]. The direct test on hollow cylindrical samples, in which water flow radially from outside to inside surfaces or vice versa, exhibits many advantages in compared with other methods: (1) a great contact surface between sample and fluid leading to a large water flow and thus a high accurate measurement; (2) reduction of the test duration due to a small sample thickness; (3) leakage reduction and (4) easy saturation of the sample [5,15,17,44]. This method is adopted in this study to evaluate the water permeability of concrete.

Chloride ingress and diffusion in concrete are controlled by different chemical and physical transport mechanisms, which are classified into five categories: diffusion, permeation, migration, convection and capillary suction [56,59]. Different techniques have been developed and standardised to measure the diffusion coefficient and the chloride migration on the concrete specimen in the laboratory tests: Rapid Chloride Permeability Test (AASHTO T277 [1], ASTM C1202 [8]); non steady-state diffusion test (NT BUILD 443 [49], ASTM C1556 [9]); electrical migration test (NT BUILD 492 [48]); ponding test (AASHTO T259 [2]). These laboratory methods are based on Fick and Nernst-Planck equations [47], moisture movement [52], binding isotherms [73] and temperature variation [64]. Laboratory methods yield three different chloride diffusion coefficients: instantaneous and apparent coefficients measured from the chloride natural diffusion test and coefficient determined by rapid chloride migration (RCM). Relations exist between these three coefficients [65,68]. Besides, destructive and non-destructive techniques have also proposed for in-situ measurement of chloride concentration in concrete structure. A review and discussion of field methods can be referred in Abbas et al. [3]. Wang et al. [69] proposed a laboratory method to measure the chloride migration through a sample discs under different compressive stress levels (NT BUILD 492 [48]). In the present work, an experimental method is slightly modified from that of Wang et al. [69] to measure the chloride permeability with taking into account the compressive loading. The modification consists in the use of RCPT (ASTM C1202 [8]) to measure the rapid chloride permeability instead of the chloride migration carried out by Wang et al. [69].

Chloride diffusion through a cracked concrete has been widely investigated by both experimental and numerical approaches [28,29,38,42,43,58,60,70,72]. However, those studies have usually dealt with an existing macrocrack which are created by tensile stress. A few works consider the effect of uniaxial stress induced microcracks on the chloride diffusion [28,69]. Moreover, the relation between transport coefficients has been rarely reported. Bhargava and Banthia [17] modified the equation of Katz-Thompson [30] to add the stress effect on the relation between water permeability and chloride diffusivity. Djerbi et al. [28] related gas permeability to chloride diffusion coefficient via damage variable measured by ultrasound pulse velocity.

Modelling of transport phenomena in sound and cracked concrete is usually performed at a mesoscale, where the concrete includes three phases: aggregate, cement paste and ITZ. The use of classical finite element method, in which ITZ is explicitly represented by a thin layer, often leads to mesh-sensitive results when dealing with nonlinear hydromechanical coupling [62]. ITZ can also modelled by the zero thickness interface element [4,45]. This approach also needs very fine mesh, when coupling to nonlinear softening mechanical behavior, to reduce the mesh dependent result [23,57]. Bolander and Sukumar [20] showed that the lattice model exhibits the mesh-independent results, which helps to overcome the limitations of a FEM modeling. Wang and Ueda [70] firstly developed a 2D mesoscale lattice model to describe the chloride diffusion in cracks and cracked concrete. Šavija et al. [58,59] developped a 3D mesoscale lattice discretisation to describe the chloride ingress in plain and cracked concrete. However, the hydromechanical coupling was excluded in those lattice models.

This study focuses firstly on the effect of compressive load induced microcracks on water permeability and chloride diffusivity of concrete by experimental investigations and hydromechanical lattice modelling at a meso description. Secondly, empirical relation between these two transport coefficient are proposed. Two industrial ordinary concretes were considered. Five stress levels 0, 0.2, 0.4, 0.6 and 0.8 and four levels 0, 0.3, 0.5 and 0.7 of the compressive strength were considered during water permeability and chloride diffusion tests, respectively. Hollow cylindrical samples were used in water permeability tests. Whereas, the chloride diffusion coefficient is evaluated by the Rapid Chloride Permeability Testing on a cylindrical sample. Mesoscopic hydromechanical lattice modeling consists of the spatial discretisation and the constitutive behaviors for different components (aggregate, mortar and ITZ). Discretization is based on a dual element network: Delaunay triangles for mechanical elements and Voronoi polygons for conduit elements. Aggregate is assumed to be elastic, while cement paste and ITZ are represented by an elastic-damage with softening model. The water seapage and chloride diffusion are respectively described by Darcy and Fick second laws for intact material. Cubic law is used to model the fluid flow in a crack, while the experimental result of Djerbi et al. [29] is implemented into lattice model for cloride diffusion in a crack. The mechanical and transport properties of three components are taken from the open litterature, as well as calibrated from the experimental results performed in this study. Both experimental and numerical results allow to elaborate a relation between water permeability and chloride diffusion coefficients. Numerical simulation reproduces well measurement on the sample and also helps to extrapolate the experimental results to 100% of the compressive strength. This also indicates that the mesoscopic lattice model is quite appropriated and helpful for predicting the durability of reinforced concrete structure.

2. Experimental programs

2.1. Materials

Two normal strength concretes C_1 and C_2 were investigated, which are commonly used in construction and building. The mixture proportion of these concretes is shown in Table 1. C_1 is usually used for substructures, while C_2 is essentially used in the main bearing structures. The particle-size distribution of aggregate is determined by a sieve analysis in accordance to ASTM C136 [10], in which the fine aggregate is natural river sand and the coarse aggregate is crushed gravel with the maximum size of 12.5 mm. The aggregate is designed according to the requirement of ASTM C33 [6]. Portland cement is made with respect to the standard specification ASTM C150 [7].

Prior to the main tests (i.e. water and chloride permeabilites of concretes under compressive stress shown in Sections 2.2 and 2.3), basic mechanical and transport properties of concretes and cement

Table 1
Mixture proportion for 1 m^3 and mechanical propertie of two concretes.

Mixture ID	Cement (kg)	Fine aggregate (kg)	Coarse aggregate (kg)	Water (kg)	w/c
C_1	395	695	1231	170	0.43
C_2	472	626	1197	170	0.36

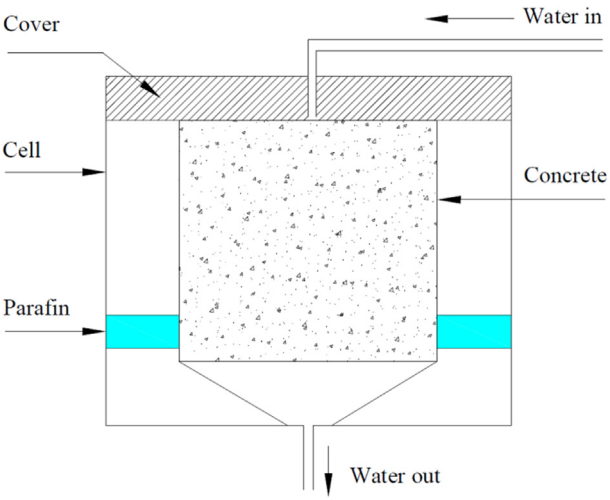

Fig. 1. Water permeability test principle according to standards BS EN 12390-8:2019 and DIN 1048.

pastes at the age of 28 days, including Young modulus E, tensile strength f_t, compressive strength f_c, water permeability K and chloride diffusivity D were characterized. Three mechanical properties (E, f_t, f_c) are determined by the classical tests [11–13]. The chloride diffusivity D was measured by the test method shown in Section 2.3

Table 2
Measured mechanical macroscopic parameters of two concretes C_1 and C_2.

Parameters	C_1	C_2
Young's modulus E (GPa)	31.4	34.3
Tensile strength f_t (MPa)	2.52	2.82
Compressive strength f_c (MPa)	41.7	52.4
Water permeability K (m/s)	1.15E−09	1.10E−09
Chloride diffusivity D (m^2/s)	8.02E−12	6.30E−12

for the case without stress. On the contrary, the device for the measurement of water permeability under stress described in Section 2.2 can not be use to measure the water permeability K for the case without stress due to the leakage problem. The water permeability was evaluated on specimen of size 150 × 150 × 150 mm according to the standards BS EN 12390–8:2019 and DIN 1048. The principle of this test is shown in Fig. 1. The water permeability is the average value resulted from three tests with three hydraulic heads 3, 4, 5 atm applied on the top surface of the specimen.

The basic properties are recapitulated in Table 2 for two concretes C_1 and C_2, as well as two corresponding cement pastes with w/c ratio 0.43 and 0.36 in Table 3. The w/c ratios were chosen to achieve the required compressive strengths of two considered concretes C_1 and C_2 (see Table 2).

2.2. Water permeability test

Hollow cylindrical concrete specimen, with 200 mm length, 100 mm external diameter and 50 mm internal diameter, were prepared for water permeability test (Fig. 2). After casting for 24 h, samples were total immersion in water at 20 °C during 28 days before the tests. Two top and bottom surfaces of specimen were sealed with rubber O-rings using a silicone glue to prevent the leakage during the test. Water permeability tests were carried out at the ambient temperature condition.

The method proposed by Banthia et al. [15] and Amriou and Bencheikh [5] is used to evaluate the water permeability of concrete with uniaxial compressive stress. The permeability measurement needs a measuring cage, a water tank and measuring devices (Fig. 1c). Measurement devices include water inlet gauges, water pressure sensors, load gauges, electronic scales, dataloger and computer. The computer automatically controls the load levels and records the mass of water flowing out. A water pressure upper than the atmospheric pressure is applied on the outer wall, while the atmospheric pressure is maintained on the inner wall to create a pressure gradient and a radial flow from the outer to the inner wall of the sample. The capacity of the device allows a maximal water pressure 10 atm on the outer wall.

Specimens were installed in water-proof cages. Water was filled in the cage to remove air. The lid of the cage was tightened with bolts and rubber O-rings. The specimen was placed in the cage such that water would permeate through 25 mm of thickness from the outer wall to the inner hollow core. The water in the hollow core is then drained out to a collection reservoir and water mass was measured continuously and accurately using an electronic

Fig. 2. Hollow cylindral concrete samples for water permeability test (a, b); permeability cell (c).

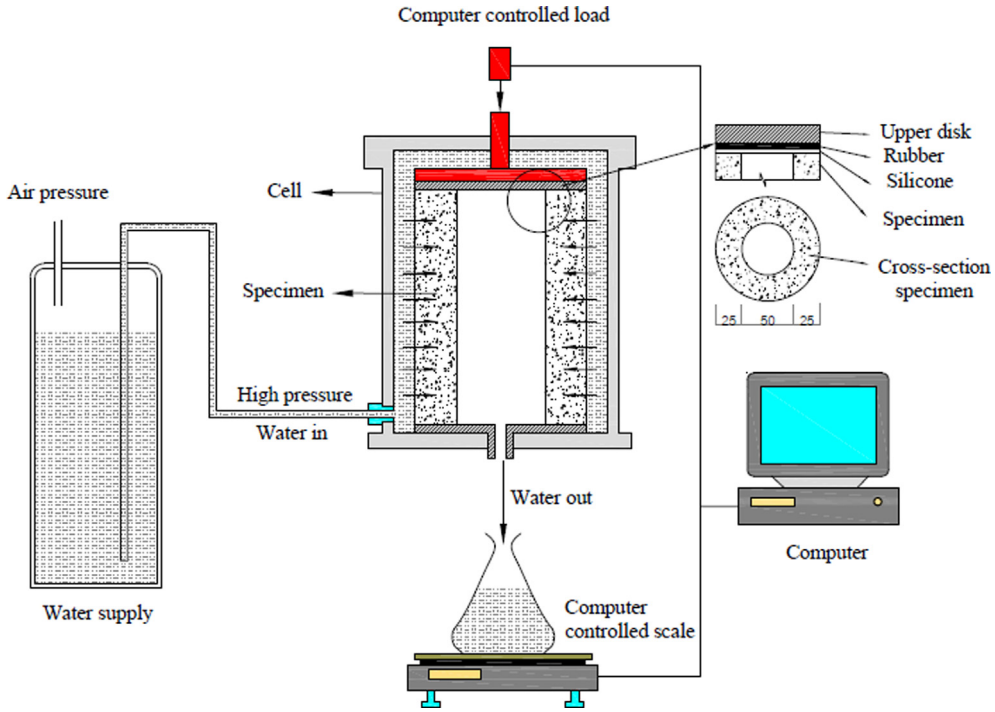

Fig. 3. Experimental set up for water permeability test under compressive stress.

scale connected to a computer. The cage was put in a testing machine to apply a certain compressive stress on the specimen during the test. The load relaxation could occur in the machine with time, and this drop in load was offset by applying an additional force to achieve an experimental compressive stress. This machine was connected to the computer to set up automatically the mechanical load (Fig. 3).

The water masse rate (m^3/s) was recorded when the flow was stable. Water permeability measurements were taken place for a period of 16 h, when the water pressure gradient was maintained constant. Three pressures 3, 4 and 5 atm were applied on the outer surface, while the atmospheric pressure is always maintained on the inner wall. The permeability was measured at the four compression stress levels σ/σ_c = 0.2, 0.4, 0.6 and 0.8 (σ_c is the compressive strength). To avoid the water leakage via top and bottom surfaces, a compressive stress σ/σ_c = 0.1 is sufficient for the case where the water pressure applied on the outer wall is 0.5 atm. However, the leakage undoubtedly occurs for the case σ/σ_c = 0.0. As a reminder, the water permeability of concrete without stress were measured according to the standards BS EN 12390–8:2019 and DIN 1048.

The pressures 3, 4 and 5 atm are equivalent to water column heights of 30, 40 and 50 m respectively. Therefore, the test condition represents the marine structures in which the depth of the substructure varies from 30 to 50 m from the free surface of water. The substructure is subjected to both the environmental impact and service loading. Moreover, the water pressure imposed on the outer surface does not present any risk for the sample wall breaking.

For each permeability test, the coefficient of water permeability K_w (m/s) is calculated by Darcy's law

$$K_w = \frac{Q.l}{A.H} \quad (1)$$

where Q is the rate of water flow (m^3/s), l is the thickness of a specimen (l = 25 mm), A is the seepage area (m^2) (A = 0.0628 m^2), H is the pressure head (m).

The water permeability coefficients measured over a period of 16 h for different water pressure levels and for different compressive stress levels recapitulated in Table 4 and Table 5 for concretes C_1 and C_2, respectively. It is worth noting that the average coefficient of water permeability in Tables 4 and 5 for σ/σ_c = 0 are exactly the values given in Table 3 for two concretes C_1 and C_2. They are from the same measurements according to the standards BS EN 12390–8:2019 and DIN 1048.

2.3. Chloride rapid penetration test

Initial cylindrical concrete samples with 100 mm diameter and 200 mm height were prepared and cured during 28 days. Then,

Table 4
Water of permeability coefficients with concrete C_1.

σ/σ_c	K_w (m/s) with 3 hydraulic head levels (atm)			Average coefficient of water permeability (m/s)
	3	4	5	
0.0	1.13E−09	1.16E−09	1.15E−09	1.15E−09
0.2	9.59E−10	8.69E−10	9.30E−10	9.19E−10
0.4	1.05E−09	1.13E−09	1.24E−09	1.14E−09
0.6	1.38E−09	1.61E−09	1.75E−09	1.58E−09
0.8	2.74E−09	2.99E−09	3.29E−09	3.01E−09

Table 5
Water of permeability coefficients with concrete C_2.

σ/σ_c	K_w (m/s) with 3 hydraulic head levels (atm)			Average coefficient of water permeability (m/s)
	3	4	5	
0.0	1.08E−09	1.12E−09	1.11E−09	1.10E−09
0.2	9.36E−10	9.46E−10	9.81E−10	9.54E−10
0.4	1.00E−09	1.09E−09	1.27E−09	1.12E−09
0.6	1.23E−09	1.45E−09	1.74E−09	1.47E−09
0.8	2.49E−09	2.89E−09	3.18E−09	2.85E−09

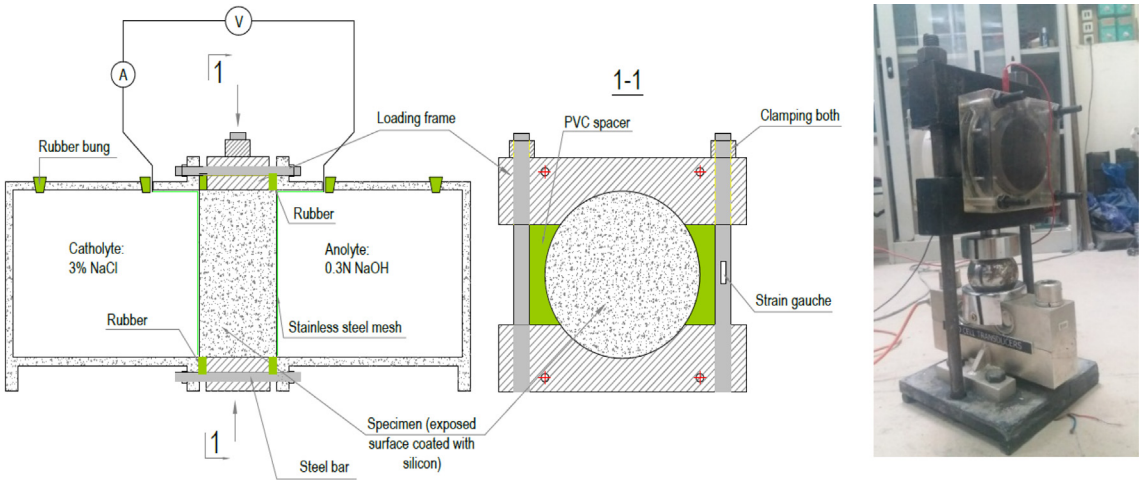

Fig. 4. Experimental set up for RCPT under compressive stress.

concrete discs of 50 mm were cut off from the initial samples at their central position by a water-cooled diamond saw. The thickness of each disc specimen was measured by a digital calliper with an accuracy of 0.1 mm. Two epoxy resin coats were used to seal the lateral surface of concrete discs to ensure one dimensional chloride flow during the test. Specimens were saturated by placing in a vacuum container by ensuring that two end surfaces were exposed. The pressure was decreased less than 1 mmHg and the vacuum was kept for four hours before allowing air to introduce. Then, water was introduced into the container to immerse the specimen for 18 ± 2 h before taking out and placing the specimen in the test setup.

Once the epoxy resin coat had hardened, the specimens were loaded at a constant rate of 1.23 ± 0.1 kN/s until the failure. The average load corresponding to the failure of three samples was taken as the maximum load for each type of concrete, which is considered as the ultimate stress σ_{max} (or σ_c). To create a state of direct compression, stress is generated by a downforce from bolts and adjusted by a load cell (see Fig. 4). After reaching the target value of load, two chambers containing NaCl and NaOH solutions were installed. Four stress levels were considered: σ/σ_{max} = 0; 0.3, 0.5 and 0.7. For the case without stress, we did not need tighten the bolts to create the compression. Then, the test process was performed to measure the chloride ion permeability by following the standard Rapid Chloride Permeability Testing (RCPT) (ASTM C1202 [8]). The specimen was placed between two acrylic cells, one was filled with a 0.3 mol/l NaOH solution and other with a 3% NaCl solution. The cells were connected to a 60-V power source. Test device is connected to a computer system to determine automatically the total amount of electrical energy transmitted through the sample. The current was measured and recorded during 6 h and then the total charge passed through the sample was computed by integrating the current over time (RCP).

Berke and Hicks [19]'s emperical formulation is used to correlate the RCP value and the chloride diffusion coefficient (D)

$$D = 0.0103\ (\mathrm{RCP})^{0.84}\left(10^{-12}\mathrm{m}^2/\mathrm{s}\right) \quad (2)$$

where the unit of RCP is Coulombs.

It is worth noting that this formula was obtained for the case without loading, where the rapid chloride permeation occurs uniformly on two sample surface [19]. In this study, the frame loading is designed similarly to that proposed by Wang et al. [69], which ensures a quasi-uniform stress distribution within the sample. This allows also a quasi-uniform distribution for the rapid chloride permeation. Moreover, the formula is fitted from the test data that the dispersion is not negligeble. Therefore, we assume that empirical law of Berke and Hicks [19] is also valid for the case with stress in this study. Obviously, it is interesting to check this assumption in further studies.

Table 6 recapitulates the RCP values and the chloride diffusion coefficients (D) resulted from the formula for two concrete types C_1 and C_2 for different loads. The chloride diffusivity (D) of two concretes corresponding to σ/σ_c = 0 are already given in Table 2. These values for cement paste with two w/c ratios 0.43 and 0.36 were also measured and shown in Table 3 for the case without loading condition.

Table 6
RCP values and chloride diffusion coefficients (D) of two concretes C_1 and C_2.

Stress levels σ/σ_{max}	Concrete C_1			Concrete C_2		
	RCP (Coulombs)		D (m^2/s)	RCP (Coulombs)		D (m^2/s)
0	2679	2767	8.02E−12	2076	2076	6.30E−12
	2753			1948		
	2868			2203		
0.3	2346	2332	6.95E−12	1857	1723	5.39E−12
	2239			1749		
	2410			1564		
0.5	3269	3241	9.16E−12	2459	2452	7.25E−12
	3426			2374		
	3028			2523		
0.7	3846	3759	1.04E−11	2769	2918	8.39E−12
	3755			3018		
	3676			2967		

3. Hydromechanical lattice models

Lattice discretisation for hydromechanical (HM) coupling through a 2D domain consists in a dual network of Delaunay triangles and Voronoi polygons, which are built from a randomly generation of nodes [14,53] (Fig. 5a). The 1D transport and mechanical elements are respectively placed along the edges of the Voronoi polygons and the Delaunay triangles. The middle cross-sections of the mechanical lattice elements are the length of the corresponding transport elements and conversely the cross-section of the transport lattices elements are the length of the corresponding mechanical lattice elements. The generation of nodes within a considered domain S_d is controlled by two parameters: spatial density ρ_n and the minimum distance between nodes d_{min}. The density of

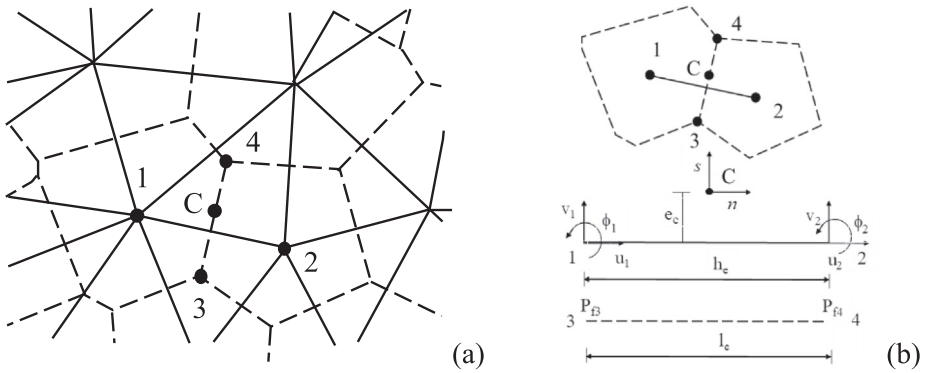

Fig. 5. HM lattice discretisation: (a) Dual Voronoi and Delaunay tessellations; (b) coupling between a single transport element and a single mechanical element.

nodes ρ_n describes the distribution of the distances between nodes, which is a function of the number of nodes N_n and the minimum distance $d_{\min}$ such as

$$\rho_n = \frac{N_n d_{\min}^2}{S_d} \tag{3}$$

The values of ρ_n and $d_{\min}$ are taken sufficiently large to ensure the convergence of the solution.

As a remainder, concrete at mesoscale is heterogeneous and constituted by three phases: aggregate, cement matrix and ITZ. Aggregates are assumed to be circular shape and randomly generated by Füler distribution. The generation of aggregates within a sample is controlled by three parameters: volume fraction of aggregates, their upper and lower diameters [34,36]. The lattice discretization relating to aggregate does not place randomly nodes, which are build such as the middle cross-section of the mechanical lattice elements form the boundaries between aggregate and cement matrix [21,22]. According to the computational efficiency [37,41,61,62], ITZ's thickness is setup to be 50 μm.

As seen in Fig. 5b, the HM coupling is performed at the point C, the midpoint of a common edge of two adjacent Voronoi polygons, where both transport and mechanical responses are available. Each node of mechanical element has three degrees of freedom, including two translations (u, v) and one rotation ϕ, whilst each node of conduit element has one nodal unknown either the fluid pressure P_f (for the fluid flow problem) or the chloride concentration C (for chloride diffusion problem). We respectively note $\bar{u}_e = \{u_1, v_1, \phi_1, u_2, v_2, \phi_2\}^T$ and (P_{f3},P_{f4}) as the nodal unknowns of displacement and rotation for a mechanical element (1–2) and of that of pressure for a transport element (3–4) (Fig. 5b). The relationship between the nodal unknowns of a mechanical lattice element and the displacement discontinuity at the midpoint C of the corresponding transport lattice element (i.e. the element cross-section) in the local coordinate system reads

$$\bar{u}_c = B\bar{u}_e = \begin{bmatrix} -1 & 0 & e_c & 1 & 0 & -e_c \\ 0 & -1 & -h_e/2 & 0 & 1 & -h_e/2 \end{bmatrix} \bar{u}_e \tag{4}$$

where e_c and h_e are respectively the eccentricity of the point C and the length of the mechanical element; $\bar{u}_c = (u_c, v_c)^T$ in which u_c and v_c are displacement jumps in the tangential and perpendicular direction to the mechanical elements (see Fig. 5b). In Eq. (4), e_c becomes $-e_c$ if the midpoint C is on the right hand side with respect to the mechanical element. The cross-section is determined by $A = l_e t$ where l_e is length of mid-section (i.e. the length of the corresponding conduit element), t is the out-plan thickness and $I = \frac{l_e^3 t}{12}$ is the moment of inertia.

The displacement jump at C is transformed into the strain $\varepsilon_c = \{\varepsilon_{nc}, \varepsilon_{sc}\}^T$ such as

$$\varepsilon_c = \frac{\bar{u}_c}{h_e} = \frac{1}{h_e} B\bar{u}_e \tag{5}$$

where ε_{nc}, ε_{sc} are the tangential and perpendicular components of the strain vector at the point C, respectively.

This strain relates to the stress via an elastic-damage model shown below (see Section 3.1). The rigid matrix of lattice element in the local coordinate system is determined by:

$$K = \frac{A}{h_e} B^T D_e B \tag{6}$$

where $D_e = \begin{bmatrix} \bar{E} & 0 \\ 0 & \gamma\bar{E} \end{bmatrix}$ is the elastic stiffness, $\bar{E}$ and γ are model parameters. For the stress plane condition

$$\bar{E} = \frac{E}{1-\nu}; \quad \gamma = \frac{1-3\nu}{\nu+1} \tag{7}$$

with E and ν are Young's modulus and Poisson ratio. According to Grassl et al [33], accurate numerical solution is only obtained if $\nu \leq 0.2$ (i.e. $\gamma \leq 1/3$) for a randomly generation of lattice network.

The pressure P_f in a conduit element is assumed to linearly vary between two nodes 3 and 4. Using ξ as the local coordinate with $\xi = -1$ at node 3 and $\xi = 1$ at node 4, we have

$$P_f = \frac{P_{f4} - P_{f3}}{2}\xi + \frac{P_{f4} + P_{f3}}{2} \tag{8}$$

At the point C: $P_c = P(\xi = 0) = \frac{P_{f4}+P_{f3}}{2}$.

The discretization of the chloride concentration of the chloride diffusion problem is identical to the pressure of the fluid flow problem. The discretisation of the steady-state fluid flow and the chloride diffusion equations are shown respectively in Sections 3.2 and 3.3. The proposed lattice model has been implemented in the oriented finite element package OOFEM that the solution method has been found in Patzák [54].

3.1. Mechanical constitutive equations

Aggregates are assumed to be elastic. Whereas, the constitutive damage equations proposed by Grassl et al [33] for tensile regime and by Grassl and Pearce [37] and Nguyen et al [51] for compressive regime are used in this work to model the stress–strain relation of cement paste and ITZ under both tensile and compressive loads. A brief summary of this elastic-damage model is recalled below.

The stress–strain relation in the HM coupling framework reads

$$\sigma = (1-\omega)D_e\varepsilon + b\sigma^f = (1-\omega)\,\bar{\sigma} + b\sigma^f \tag{9}$$

where ω is the damage variable; $\sigma^f = (P_f, 0)^T$; P_f the pore pressure; b the Biot's coefficient; $\sigma = (\sigma_n, \sigma_s)^T$ the stress vector; σ_n and σ_s the tangential and perpendicular components of the stress vector (with respect to the considered mechanical element orientation);

The variable ω is a function of a history variable κ, which is determined by the loading function

$$f(\varepsilon,\kappa) = \varepsilon_{eq}(\varepsilon) - \kappa \tag{10}$$

where the equivalent strain ε_{eq} is defined as

$$\varepsilon_{eq}(\varepsilon_s,\varepsilon_n) = \frac{1}{2}\varepsilon_0(1-c) + \sqrt{\left(\frac{1}{2}\varepsilon_0(1-c)+\varepsilon_n\right)^2 + \frac{c\gamma^2\varepsilon_s^2}{s^2}} \tag{11}$$

where $s = f_s/f_t$, $c = f_c/f_t$, $f_t = E\varepsilon_0$ the tensile strength, f_s the shear strength, f_c the compressive strength and ε_0 the model parameters. The loading–unloading condition is ensured by

$$f \leqslant 0, \quad \dot{\kappa} \geqslant 0, \quad \dot{\kappa} f = 0 \tag{12}$$

The softening curve is controlled by the fracture energy of pure compression G_{fc} and of pure tension G_{ft} for compressive and tensile conditions as follows

$$\sigma_n = f_t e^{\left(-\frac{\bar{e}}{\omega_i}\right)} \tag{13}$$

with $i = c$ (compression) or t (tension); $\omega_i = G_{fi}/f_i$; $\bar{e} = \| e \|$ is the equivalent crack opening; e is the crack opening vector defined by

$$e = h_e\omega\varepsilon \tag{14}$$

For pure compression or pure tension condition, $\varepsilon_s^i = 0$, thus Eq. leads to $\varepsilon_{eq} = \varepsilon_n^i$ and

$$\sigma_n^i = (1-\omega)E\varepsilon_n^i \tag{15}$$

Introducing Eqs. (15) and (13) into the yield function $f(\varepsilon,\kappa) = \varepsilon_{eq}(\varepsilon) - \kappa = 0$ results in

$$(1-\omega)\kappa = c\varepsilon_0 exp\left(-\frac{h_e d\kappa}{G_{fi}/f_i}\right) \quad (i = c,t) \tag{16}$$

which allows determining the damage variable from history variable κ.

3.2. Water transport

The fluid flow is idealised by Darcy's law due to a weak permeability of concrete's components and is considered in the steady-state condition in order to determine the homogenized permeability of concrete. In the lattice framework, the transport elements are 1D conductive pipes placed along the edges of the Voronoi polygons and their cross-section is calculated from the length of the corresponding edges of the dual Delaunay triangle. Water is assumed to be incompressible. The stationary fluid flow through a porous medium is fully described by the mass conservation equation, Darcy's law and the boundary conditions. The combination of two first equations gives the Laplace equation for the fluid pore pressure

$$\Delta P_f = 0 \tag{17}$$

The discretisation form of Eq. (17) for a conduit element is [31]

$$\alpha_e \boldsymbol{P}_f = \boldsymbol{f}_w \tag{18}$$

where $\alpha_e = \frac{h_e}{l_e}k\begin{pmatrix}1 & -1\\ -1 & 1\end{pmatrix}$ is the element conductivity; $\boldsymbol{f}_w$ is the nodal flow vector; $\boldsymbol{P}_f = (P_{f1}, P_{f2})$ is the vector of nodal fluid pore pressure; l_e and $A_t = txh_e$ are the length and the cross-section of the transport element with h_e is the length of corresponding mechanical element.

The total flow transported by a conduit element is the sum of flow through intact and damage materials. Therefore, the hydraulic conductivity is formulated by

$$k = k_0 + k_c(h_e) \tag{19}$$

where k_0 is the hydraulic conductivity of undamaged material and k_c is the hydraulic conductivity of crack resulted by damage. We assume that the fluid flow through a crack obeys the cubic law, i.e.

$$k_c = \frac{\rho g}{\mu}\frac{\bar{e}^3}{12h_e} \tag{20}$$

where g is the gravity; ρ and μ are the fluid density and the fluid dynamic viscosity.

3.3. Chloride diffusion

Chloride ingress also takes places in the transport elements, i.e. edges of of the Voronoi polygons. Fick's second law is used to describe the chloride diffusion in 1D conduit element. The discrete form of this equation in the lattice framework is

$$\boldsymbol{D}_e C + \boldsymbol{C}_e\frac{\partial C}{\partial t} = F_c \tag{21}$$

where $C = (C_3, C_4)^T$ is the nodal chloride concentration; F_c is the nodal flux; $\boldsymbol{D}_e$ and $\boldsymbol{C}_e$ are the diffusion and capacity matrix:

$$\boldsymbol{D}_e = \frac{h_e}{l_e}D\begin{pmatrix}1 & -1\\ -1 & 1\end{pmatrix} \quad ; \quad \boldsymbol{C}_e = \frac{h_e l_e}{12}\begin{pmatrix}2 & 1\\ 1 & 2\end{pmatrix} \tag{22}$$

with D is the chloride diffusion coefficient of material.

Similar to the hydraulic conductivity of a transport element, the damage induced diffusivity increase is taken into account via the crack opening for damaged element.

$$D = D_0 + D_c \tag{23}$$

where D_0 is the diffusivity coefficient of undamaged material and D_c is that of damaged material.

Two empirical relations between D_c and crack width have been proposed by Ismail et al [43] (Eq. (24)) and Djerbi et al [29] (Eq. (25)). D_c is a linear function of the crack width when the latter variable is comprised between lower and upper bounds. No increase of diffusivity occurs when the crack width is less than the lower bound due to the crack healing phenomenon of cement-based material. Šavija et al [59] implemented both equations into a transport lattice modelling and showed that the relation (25) represents the chloride diffusion within cracked concrete better than Eq. (24). In this study, the empirical model proposed by Djerbi et al [29] is adopted.

$$D_c = \begin{cases} 0 & for\ \bar{e} < 21\mu m \\ (23.84\,\bar{e} + 8.37)\times 10^{-10} & for\ 21\mu m \leqslant \bar{e} \leqslant 55\mu m \\ 1.4\times 10^{-9} & for\ \bar{e} > 55\mu m \end{cases} \tag{24}$$

$$D_c = \begin{cases} 0 & for\ \bar{e} < 30\mu m \\ 2\times 10^{-5}\,\bar{e} - 4\times 10^{-10} & for\ 30\mu m \leqslant \bar{e} \leqslant 80\mu m \\ 1.4\times 10^{-9} & for\ \bar{e} > 80\mu m \end{cases} \tag{25}$$

The three-dimensional permeability and chloride diffusivity tests presented in the previous section are modeled by 2D hydromechanical lattice model showed in this section. In the litterature, 2D mesoscopic modeling has been usually used to describe the behavior of concrete structure, in which concrete is usually

assumed also to be constituted by three phases: aggregate, cement paste and ITZ [16,25,26,32,34,35,46,62]. This simplification (3D configuration to 2D representation) must be carefully verified and validated against the test data, when using the 2D simplified model to predict the behavior of concrete structure. This is the case of this study as shown in the next section.

4. Results and discussion

4.1. Model calibration and validation

As a reminder, cement and ITZ are represented by a damage-elasticity model that the stress–strain relation is fully described by seven parameters: Young's modulus (E); Poisson ratio (ν); tensile strength (f_t); compressive strength (f_c); shear strength (f_s); pure compression fracture energy G_{fc} and pure tension fracture energy G_{ft}. Whereas, aggregate is assumed to be elastic and thus characterized only by Young's modulus (E) and Poisson ratio (ν). These two elastic parameters are related to the lattice model parameters $\bar{E}$ and γ by Eq. (7). The values of γ are taken from Grassl and Pearce [37] for three components of both concretes (aggregate, cement and ITZ). Three parameters E, f_c, f_t of two cement pastes was measured (see Table 3). Young's modulus of aggregate is assumed to be 70 GPa. This parameter of ITZ is evaluated by the following equation [37]

$$E_{itz} = \frac{1}{2}\left(\frac{1}{E_{aggr}} + \frac{1}{E_{cem}}\right)^{-1} \tag{26}$$

The remainder of parameters, including f_s, G_{fc}, G_{ft} for the cement pastes and f_t, f_c, f_s, G_{fc}, G_{ft} for ITZ were initially taken from Grassl and Pearce [37] and then adjusted to satisfy: (1) the measured macroscopic properties of two concretes shown in Table 2 and (2) the water and chloride permeability tests under compressive stress performed in this study. Only two fracture energy parameters G_{fc}, G_{ft} of both ITZ and cement matrix are adjusted. Whereas, three parameters f_t, f_c ($c = f_c/f_t$) and f_s (or $s = f_s/f_t$) of ITZ and the parameter $s = f_s/f_t$ for the cement paste are kept to be similar to those of Grassl and Pearce [37]. Table 7 recapitulates all mechanical models of different components of two concretes. These mechanical parameters are closes to those used by Grassl's studies when dealing with normal strength concrete material [33–37].

Regarding transport proprieties, aggregate is usually assumed to be impermeable in comparison to transport properties of mortar [45,58]. ITZ represents the weakness zone in concrete and thus ITZ is more permeable than the mortar. However, since ITZ phase is located at the interface between aggregates and mortar, ITZ phase is thus not percolated. Therefore, the contribution of ITZ to increase the permeability of concrete is not significant [66]. In the literature, the permeability of ITZ (K_{ITZ}) is usually assumed to be 10 times more than mortar's (K_{ce}) [45,71,74] and the chloride diffusivity of ITZ (D_{ITZ}) is 2–8 times that of cement paste (D_{ce}) [27,59,58]. ITZ transport properties have been widely estimated by using homogenization methods from the concrete properties and the volume fraction of different phases [24,50].

In this study, two coefficients λ_K^i and λ_D^i are introduced such as

$$K_{ITZ}^i = \lambda_K^i K_{ce}^i \text{ and } D_{ITZ}^i = \lambda_D^i D_{ce}^i \quad (i = 1,2) \tag{27}$$

which are determined by the adjustment between the numerical solution and the experimental data for two concrete C_1 and C_2 (i = 1,2). Besides, we assume that $K_{agg}^i = 10^{-7} K_{ce}^i$ and $D_{agg}^i = 10^{-7} D_{ce}^i$. K_{ce}^i and D_{ce}^i were directly measured (see Table 3).

4.1.1. Water permeability calibration

To determine λ_K^i, a 2D lattice model is proposed based on the experiment configuration which is shown in Fig. 6. It consists in a rectangular specimen 200 × 25 (mm^2) in which the aggregate diameter varies from ϕ_{min} = 3 mm to ϕ_{max} = 12.5 mm. Two constant pressures P_{left} and P_{right} are prescribed on the left and right sides of the model and no fluid exchange is imposed on the top and bottom surfaces. Based on the Darcy's law, the permeability of concrete is calculated by lattice model as follows

$$K_{specimen} = \frac{q_{in}}{S_{right}\left(P_{right} - P_{left}\right)} = \frac{\sum_1^n \left[K_e^{*n}\left(P_{right}^e - P_{left}^e\right)\right]}{S_{right}\left(P_{right} - P_{left}\right)} \tag{28}$$

where S_{right} = 200 mm^2 is the boundary of the right surface; q_{in} is the sum of flux entering over all conduit elements on the right boundary; P_{right}^e, P_{left}^e are the nodal pressures on the right and left nodes of the transport element e connecting to the right boundary and K_e^{*n} is the water permeability of this element.

Numerical model allows plotting a continuous evolution in permeability versus uniaxial compressive stress σ/σ_{max} from 0 to 1. By adjusting these curves against the experimental data for five stress levels (σ/σ_{max} = 0.0; 0.2; 0.4; 0.6; 0.8), the value $\lambda_K^1 = \lambda_K^2 = \lambda_K = 8$ is obtained. Fig. 7 shows the compressive stress induced permeability changes for two concretes (C_1 and C_2) obtained by water permeability test (see Section 2.2) and by lattice modelling. Test results show that the permeability slightly decreases when $\sigma/\sigma_{max} < 0.4$. Since this slight drop is not significant, this decrease in permeability due to the void closure is not taken into account in the lattice model. A uniaxial compressive stress threshold is observed between 0.4 and 0.6 times σ_{max}, beyond which the water permeability starts increasing due to the occurrence of microcracks under compression. In the literature, this stress threshold was observed about 0.3 to 0.4σ_{max} [18,40]. The threshold value is much higher for gas permeability (from 0.5 to 0.8σ_{max}). A review on the compressive stress induced (water, gas, chloride) permeability change was done by Hoseini et al [39]. Increases about 1.5 and 2.8 times compared to the initial permeability were observed at stress levels σ/σ_{max} = 0.6 and 0.8, respectively.

The lattice model with λ_K = 8 allows to reproduce the increase in permeability till 0.8σ_{max} for both concretes C_1 and C_2. In spite of the simplified assumptions, the present 2D hydro-mechanical fairly well predicts the evolution of the permeability versus the compressive stress for two considered materials.

Table 7
Summaries all mechanical model parameters.

	E(GPa)	γ (–)	f_t (MPa)	f_s (MPa)	f_c (MPa)	G_{fc} (J/m^2)	G_{ft} (J/m^2)
Aggregate	70	0.08	–	–	–		
Cement paste (C_1)	28.2	0.33	2.5	5.0	38	5×10^5	4.5×10^2
ITZ (C_1)	40.2	0.20	1.5	3.0	30	1.25×10^5	1.25×10^2
Cement paste (C_2)	29.5	0.33	2.8	5.6	45	5.5×10^5	5.2×10^2
ITZ (C_2)	41.5	0.20	1.5	3.0	30	1.25×10^5	1.25×10^2

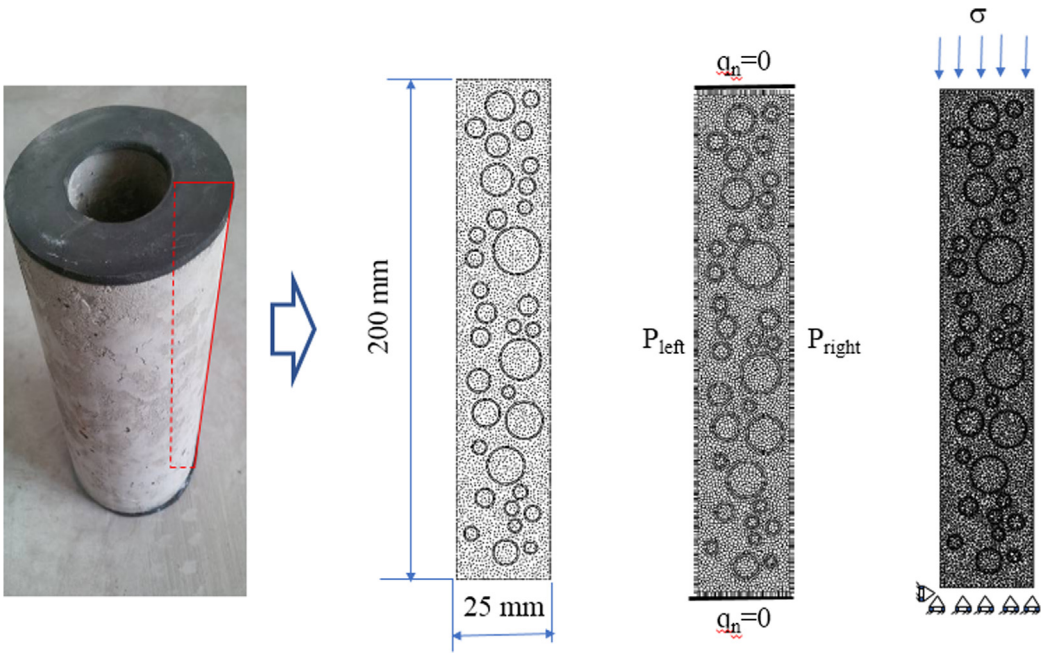

Fig. 6. Lattice model for water permeability test under compressive stress.

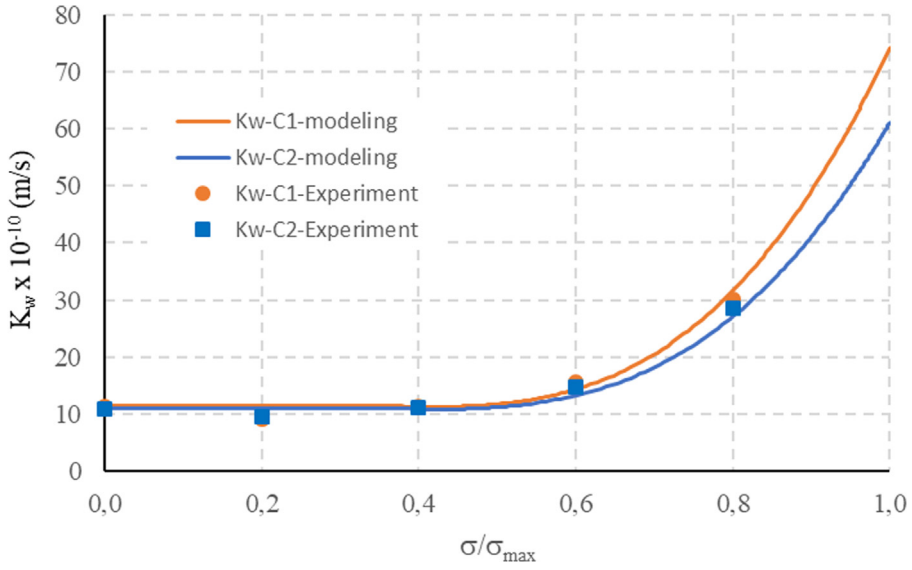

Fig. 7. Evolution of permeability versus stress level for two concretes C_1 and C_2 (experimental and modeling results).

To the best of the authors' knowledge, the experimental investigation on the change in water permeability for a compressive stress close to σ_{max} has not done yet for concrete material. However, the permeability measurement during a triaxial test has widely performed for the brittle rock material, which shows generally: (1) slight decrease in permeability due to the void closure following by a constant value of permeability corresponding to the elastic stage; (2) progressive increase in permeability from the yield stress to the peak stress (nonlinear plastic hardening or pre-peak stage) due to the occurrence of microcrack; (3) considerable increase in permeability corresponding to the post-peak or plastic softening stage where microcracks coalesce to form the macrocrack (percolated micro-crack network) and (4) a progressive increase in permeability during the residual stage [63,67,75]. Concrete is much more heterogeneous than rock material. The weakness zone at the interface between the aggregate and the cement paste make concrete easier to be damaged than homogeneous rock by bond crack when subjecting to the compressive stress. This might lead to a trend of permeability change of the plain concrete different to that of the rock. However, as reviewed by Hoseini et al [39], the variability of water and gas permeability change under compressive stress is significant. The mesoscopic lattice modeling of the ordinary concrete under compressive stress shows that (1) the cracks are mainly initiated at the aggregate-matrix interface within the hardening stage; (2) then ITZ becomes strongly damaged and cracks also occur in the mortar at the peak stress; (3) the cracks localise into two shear bands (macrocracks) at the softening stage [37,51]. This explains a progressive increase in permeability evidenced by lattice modeling from $\sigma/\sigma_{max} \sim 0.5$ (yield stress) to 1.0 (peak stress) in this study.

4.1.2. Chloride diffusivity calibration

To determine the chloride diffusivity in the numerical modeling, two materials are considered including the heterogeneous concrete with three phases (aggregate, mortar and ITZ) and a fictitious homogeneous material with the homogeneous chloride diffusion coefficient provided in Table 6 by the measurement. At a compressive stress level σ/σ_{max}, hydromechanical lattice modeling is performed on the 2D sample described in Fig. 8. A chloride concentration C_{left} = 0.35 is applied on the left side and non-exchange condition is prescribed on the other three edges. The evolution of chloride concentration $C_{right}(t)$ on the right side of the sample is followed. $D^i_{ITZ} = \lambda^i_D D^i_{ce}$ (or the coefficients λ^i_D) (i = 1,2) are determined by adjusting the curve $C_{right}(t)$ obtained for the heterogeneous concrete in comparison with that of the fictitious homogeneous material. Herein, C_{right} is the average value of nodal chloride concentration on the right nodes of all conduit elements connecting to the right boundary. As shown in Fig. 9, a good accordance between two curves of $C_{right}(t)$ for the heterogeneous concrete and the fictitious homogeneous material is found for both two concretes C_1 and C_2 with the choice $\lambda^1_D = \lambda^2_D = \lambda_D = 2.7$. This value is found in the range observed by previous studies [27,58,59].

To determine the macroscopic chloride diffusivity of a concrete sample (heterogeneous material) at a stress level σ/σ_{max}, the curve $C_{right}(t)$ is firstly computed. Secondly, the coefficient of chloride diffusion of the fictitious homogeneous sample is adjusted in a way that the curve $C_{right}(t)$ fits to the curve of the heterogeneous sample. This chloride diffusivity obtained by this adjustment is the macroscopic coefficient (D) of concrete sample corresponding to the loading σ/σ_{max}. D is computed for σ/σ_{max} = 0, 0.1, 0.2, 0.3, 0.4, 0.5, 0.6, 0.7, 0.8, 0.9 and 1.0 and the result shown in Fig. 10. As a reminder, the actual lattice model does not predict a decrease of D for a weak compressive stress due to the void closure as shown by experimental result (σ/σ_{max} = 0.3). However, this decrease is slight in comparison with the increase of D for high stress level (σ/σ_{max} > 0.3). The numerical result shows the increase in diffusivity starts from $\sigma/\sigma_{max} \sim 0.5$, which is coherent to the permeability increase in Fig. 9. A slight increase is observed from σ/σ_{max} = 0.5 to 0.7 and then a linear increase from σ/σ_{max} = 0.7 to 1.0. Two concretes C_1 and C_2 exhibit a similar trend of evolution in chloride diffusivity. Once again, the proposed 2D lattice model is in a good agreement with the test data for the chloride diffusivity versus the compressive stress.

4.2. Damage induced permeability and chloride diffusivity changes

4.2.1. Damage versus stress level

Concrete sample is modelled at a mesoscale with three different phases: elastic aggregate and mortar, ITZ represented by an elastic-damage model. Aggregate is much solid than ITZ and cement paste. Under a sufficient compressive stress level, the concrete can be

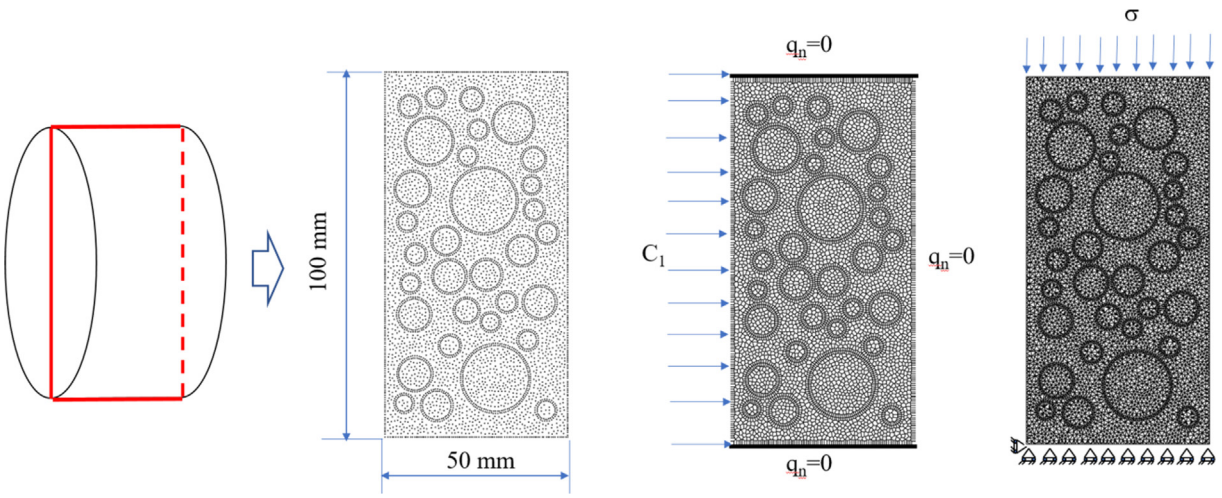

Fig. 8. 2D lattice model for chloride diffusion test under compressive stress.

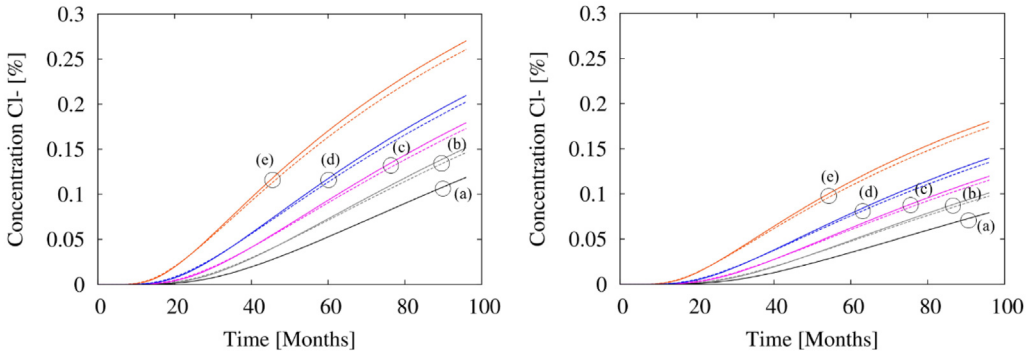

Fig. 9. Evolution of chloride concentration $C_{right}(t)$ under five stress levels σ/σ_{max} = 0.0 (a); 0.3 (b); 0.5 (c); 0.75 (d) and 1.0 (e) in which solid line: heterogeneous material and dash line: homogeneous material.

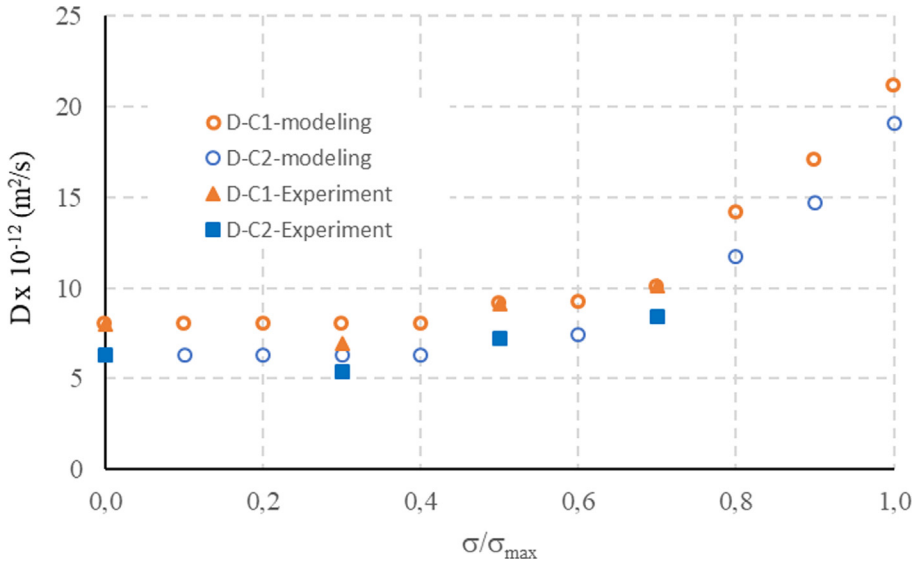

Fig. 10. Evolution of chloride diffusivity versus stress level for two concretes C_1 and C_2 (experimental and modelling results).

damage, which initiates and develops firstly in the ITZ elements and then in the cement matrix. When the uniaxial compressive stress varies from 0 to the compressive strength, the concrete sample passes two stages: elastic behaviour ($\sigma/\sigma_{max} < \sim 0.5$) and plastic hardening (pre-peak) ($0.5 < \sigma/\sigma_{max} < 1.0$). If the loading is controlled by the displacement, the softening and residual behavior will be observed after the peak [51]. The damage variable d of a concrete sample is introduced as follows

$$d = 1 - \frac{E_\sigma}{E_0} \tag{29}$$

where E_σ is the unloading modulus corresponding to the stress level σ; E_0 is the initial elastic modulus ($E_\sigma = E_0$ if $\sigma/\sigma_{max} < 0.5$). As a remainder, the proposed model does not produce the irreversible (plastic) strain when unloading on the concrete specimen since the aggregate is elastic whilst cement matrix and ITZ are modelled by an elastic-damage model. Therefore, the unloading modulus is identical the secant modulus (see Fig. 11 for concrete C_1).

The computation of damage variable as a function of stress by using the geometry model described in Fig. 8 is reported in Fig. 12. Lattice modeling shows that d starts being different to zero at $\sigma/\sigma_{max} \sim 0.47$ for concrete C_1 and ~ 0.49 for concrete C_2. These values of stress level corresponding to the thresholds where the permeability starts increasing. The increase of d exhibits a slight rate when $\sigma/\sigma_{max} < 0.7$ and the increase rate increases with the increase of the stress level. At the highest stress level $\sigma/\sigma_{max} = 1.0$, $d = 0.26$ for concrete C_1 and $d = 0.24$ for C_2, which are lower than 1. Indeed, at $\sigma/\sigma_{max} = 1$, the concrete specimen fails at numerous elements (where $\omega = 1$), which forms one or two macrocracks (so-called also by shear bands). However, the whole sample does not fail completely, which resists to the low compressive stress due to the friction of the macrocracks. This is the typical behaviour of a softening plastic material. Fig. 11 shows the classical (axial) stress–strain curve of the concrete sample under uniaxial condition (for concrete C_1). The compressive loading is performed by imposing a constant displacement rate. As seen, the specimen does not

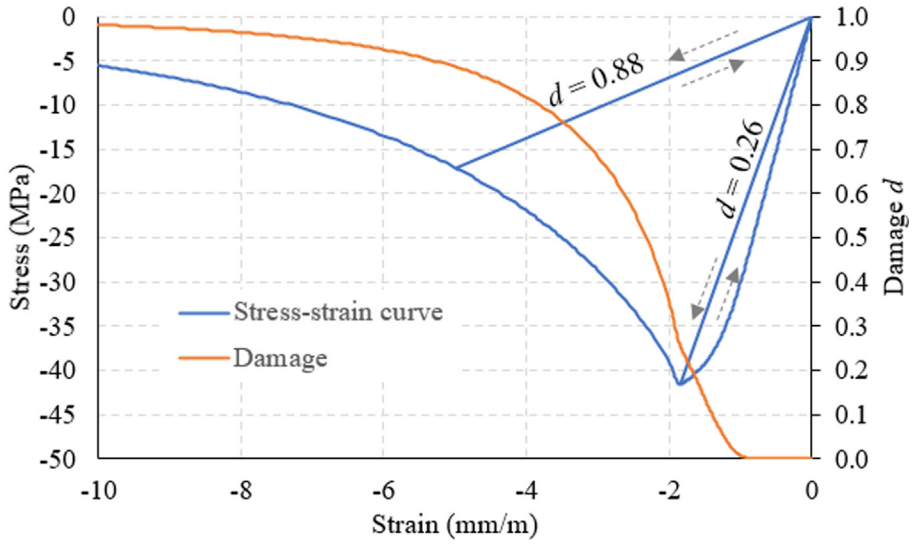

Fig. 11. Evolution of stress and of damage variable during uniaxial compression test of concrete C_1.

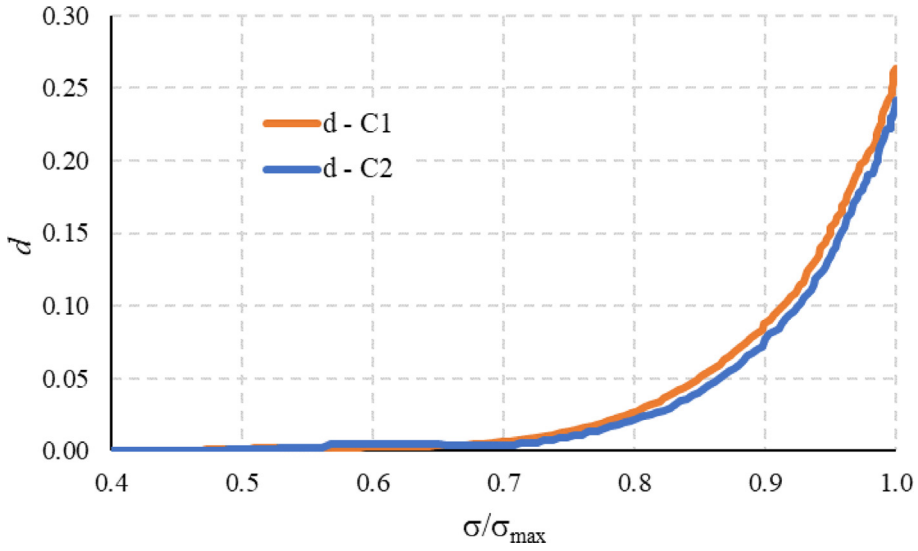

Fig. 12. Evolution of damage variable versus stress level for two concretes C_1 and C_2.

fail immediately at $\sigma/\sigma_{max} = 1$ and it exists the softening stage. The damage variable d reaches 1 when the axial strain (i.e. imposing displacement) is large enough.

4.2.2. Permeability and chloride diffusivity versus damage

The evolutions of transport properties (K_w, D) and the damage variable d relate to the stress level σ/σ_{max} (see Figs. 7, 10, 12). Therefore, it is possible to relate the transport properties (K_w, D) to damage variable d. Figs. 13 and 14 plot the relationships between K_w and d, as well as D and d for two concretes C_1 and C_2. The result shows an important increase rate of K_w and D when the damage variable is weak ($d < 0.02$) followed by progressive increase in permeability K_w and in chloride diffusivity D. The appearance of the macrocrack (coalescence of microcracks or percolation of microcrack-network) usually takes place in the post-pic (softening behaviour) state [75]. This might be a reason why lattice modeling does not obtain a considerably increase in permeability when σ reaches σ_{max}. Besides, the chloride diffusivity of a crack is bounded by lower and upper limits (see Eq. (25)). Thus, there is not a dramatically increase in the coefficient of chloride diffusion even if at the percolation threshold of the microcrack-network (appearance of macrocrack).

As seen in Figs. 13 and 14, the variations of K_w and D versus d can be fitted by a power law such as

$$\frac{K_w(d)}{K_{0i}} = A_i d^{m_i} \quad \text{and} \quad \frac{D(d)}{D_{0i}} = B_i d^{n_i} \quad (i = 1,2) \tag{30}$$

where $i = 1$ for concrete C_1 and $= 2$ for concrete C_2; $K_{0i} = K_w(d = 0)$; $D_{0i} = D(d = 0)$; A_i, B_i, m_i, n_i are fitting coefficients: $A_1 = 9.8113$; $m_1 = 0.3325$; $A_2 = 8.3254$; $m_2 = 0.3029$; $B_1 = 3.2890$; $n_1 = 0.1760$; $B_2 = 3.9211$; $n_2 = 0.1938$.

4.3. Relationship between permeability and chloride diffusivity

Eq. (30) allows deducing a power relation between the water permeability K_w/K_0 and the chloride diffusivity D/D_0 via the damage variable d such as

$$\frac{K_w}{K_{0i}} = A_i B_i^{\frac{n}{m}} \left(\frac{D}{D_{0i}}\right)^{\frac{m}{n}} = E_i \left(\frac{D}{D_{0i}}\right)^{t} \quad (i = 1,2) \tag{31}$$

where $E_1 = 1.035$; $t_1 = 1.8892$; $E_2 = 0.9840$; $t_2 = 1.5630$.

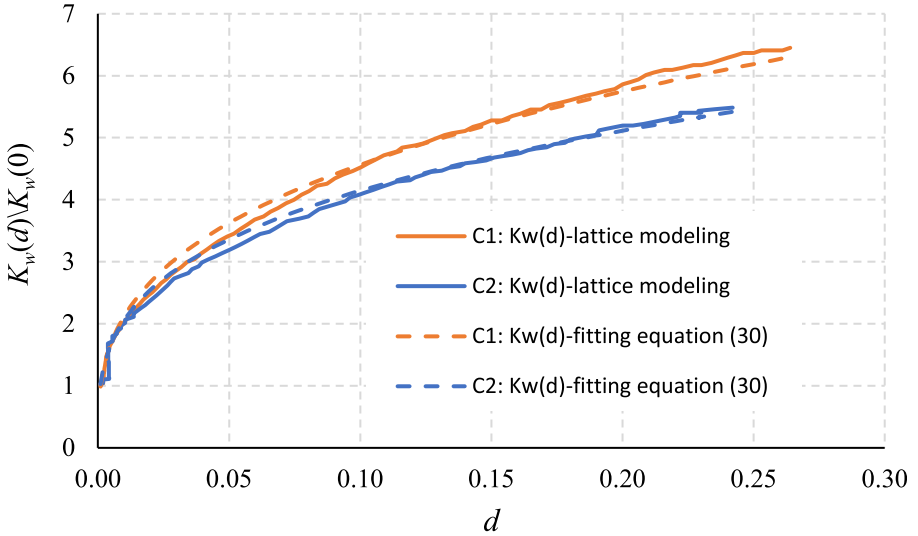

Fig. 13. Relation between water permeability K_w and damage variable d for two concretes C_1 and C_2.

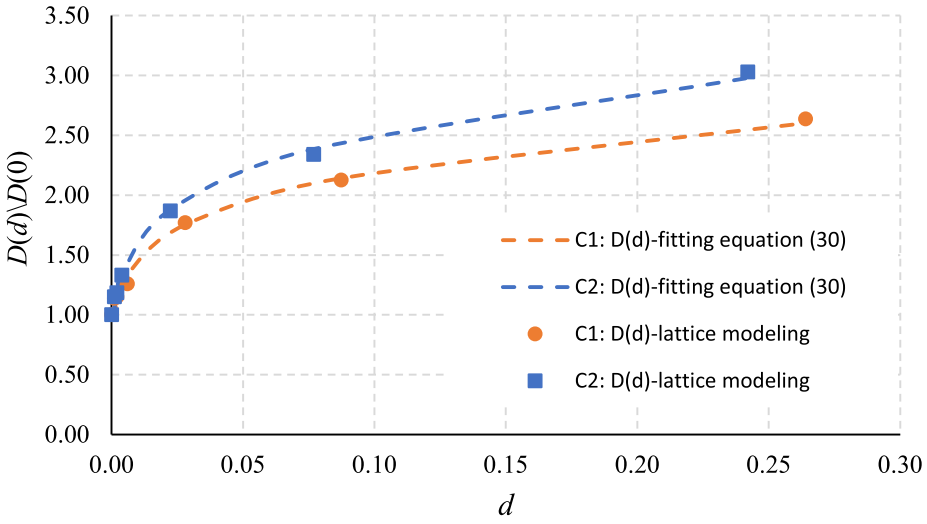

Fig. 14. Relation between chloride diffusivity D and damage variable d for two concretes C_1 and C_2.

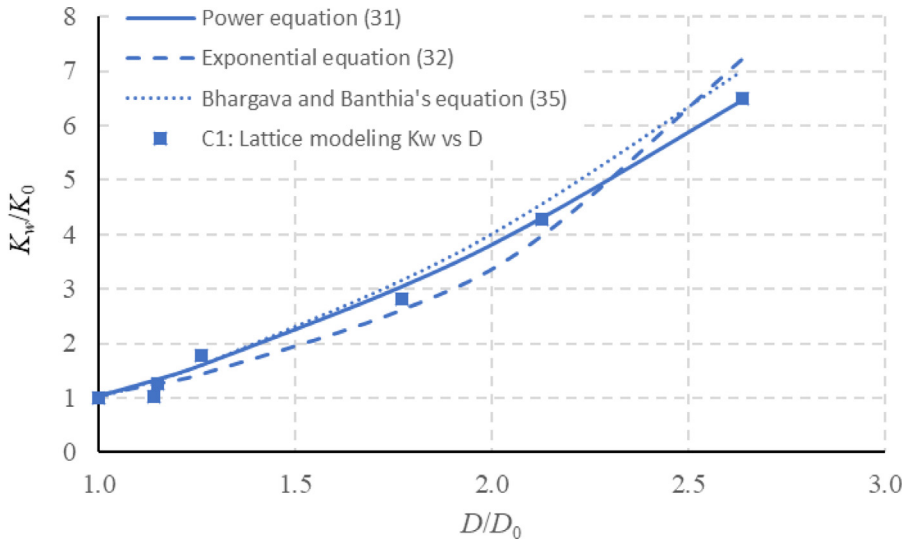

Fig. 15. Relation between K_w/K_0 and D/D_0 for concrete C_1.

The variation of K_w/K_0 versus D/D_0 obtained by the proposed lattice model can be also fitted by an exponential relation (see Fig. 15)

$$\frac{K_w}{K_{0i}} = F_i \exp\left(H_i \frac{D}{D_{0i}}\right) \quad (i = 1, 2) \tag{32}$$

where F_1 = 0.3299; H_1 = 1.1699; F_2 = 0.4390; H_2 = 0.8781. Exponential regressions were also proposed by Djerbi et al. [28] for plain and high-performance concretes to relate the gas permeability to the chloride diffusion coefficient.

Based on a theoretical analysis, Bhargava and Banthia [17] proposed the following relation between the water permeability and chloride diffusivity

$$K_w = HF^{0.5}S^{0.5}D \tag{33}$$

where F is a factor to consider the effect of fiber content in concrete, which is expressed by the ratio between the permeability coefficient of the fiber reinforced concrete and the water permeability coefficient of the concrete without fiber. When considering only normal strength concrete (F = 1), the formulation becomes

$$K_w = HS^{0.5}D \tag{34}$$

where S is the effect of stress on water permeability of concrete that is expressed as the ratio between the permeability coefficient of concrete under stress and without stress. H is a factor to consider the correlation between the permeability coefficient and the chloride diffusion coefficient in unstressed state $H = K_0/D_0$. Hence, H = 142.93 (m^{-1}) for concrete C_1 and H = 175.13 (m^{-1}) for concrete C_2.

Re-writing Eq. (33) for K_w/K_0 and D/D_0

$$\frac{K_w}{K_{0i}} = \left(\frac{D}{D_{0i}}\right)^2 \quad (i = 1, 2) \tag{35}$$

The fitting (power and exponential function) and Bhargava and Banthia [17] relations are plotted in Figs. 15 and 16 for concretes C_1 and C_2. The comparison shows that the power function is the best approximation of the lattice modelling results for the range of loading σ/σ_{max} from 0 to 1 for both concretes C_1 and C_2. The exponential function is not as good as the power function but

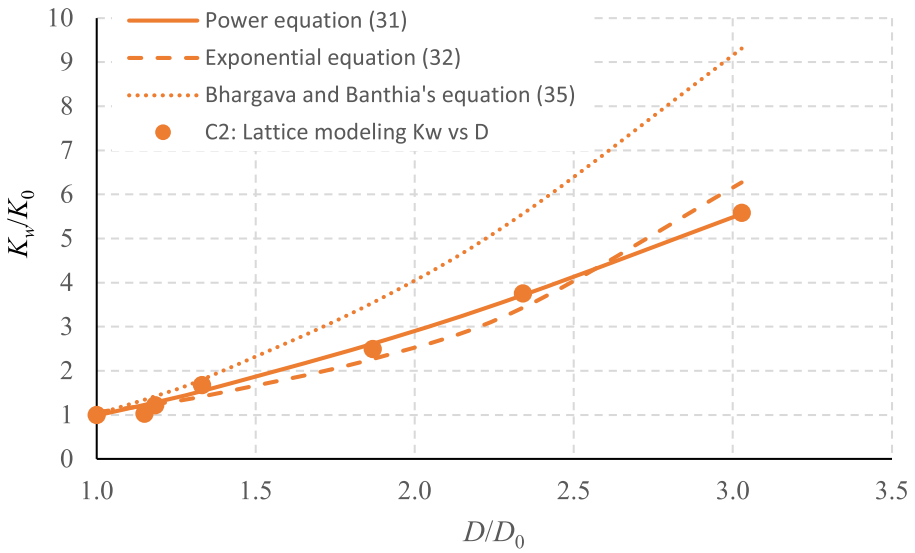

Fig. 16. Relation between K_w/K_0 and D/D_0 for concrete C_2.

acceptable. The Bhargava and Banthia [17]'s relation is close to the lattice modeling (and thus the experiment result) for C_1 with $\sigma/\sigma_{max} < 0.9$. However, this empirical formulation is far from the lattice modelling result (and experiment data) for concrete C_2.

The result from two considered concretes is useful for a preliminary assessment of the transport properties of a normal strength concrete, particularly the case that the concrete composition is close to C_1 and C_2. According to the power Eq. (31), two relations between the water permeability and the chloride diffusivity are not similar for two considered concretes C_1 and C_2. Hence, the result in this study can not be applied directly to other concrete. However, the proposed lattice model can help to predict the water permeability and the chloride diffusivity under a service loading for a specific concrete if its compositions and its basics properties are known (e.g. Young modulus, compressive and tensile strengths, water permeability, chloride diffusivity).

5. Conclusions

This study proposes relations between the water permeability and the chloride diffusivity of two ordinary concretes under uniaxial compressive stress condition from unstressed state to the compressive strength. Experimental approach and hydro-mechanical lattice modeling were investigated to determine the transport properties. Water permeability and chloride diffusivity were measured by using standard methods: direct test on a hollow cylindrical sample for water permeability and Rapid Chloride Permeability Test for chloride diffusion coefficient measurements. Water permeability were measured under five stress levels (σ/σ_{max} = 0, 0.2, 0.4, 0.6 and 0.8). Four stress levels (σ/σ_{max} = 0, 0.3, 0.5, and 0.7) were applied when measuring the chloride diffusivity. The experimental results show a slight decrease of transport properties of two concretes when the compressive stress is small ($\sigma/\sigma_{max} < 0.4$) and start increasing about the stress threshold ($\sigma/\sigma_{max} \sim 0.5$).

Hydro-mechanical lattice modelling is proposed to cover a largest range of compressive stress (σ/σ_{max} from 0 to 1). In such a model, concrete is considered at a mesoscale and is constituted by three different phases: elastic aggregate; mortar and ITZ are represented by a damage model with softening behaviour. The hydromechanical coupling is performed by Biot's theory. Mechanical and transport properties of these three phases are estimated based on the test data. The proposed model reproduces the diffusion phenomena of water and chloride within concrete under compressive stress observed by the tests. Damage variable is calculated as a function of stress level. The power formulation is proposed to relate the transport properties to the damage variable. This allows to obtain the relation between water permeability and chloride diffusivity. Both power and exponential functions can be used to approximate that relations for two considered concretes. However, the power formulation is the best approximation. It helps to determine one property if the other is available. Despite the limitation of the present hydro-mechanical lattice model is the 2D representation, it reproduces fairly well the test observation for both water permeability and chloride diffusivity tests.

Two considered concretes in this study C_1 and C_2 have been widely used for bride construction based on the American standard (AASHTO LRFD Bride Design Specification), where C_1 is usually used for substructures while C_2 is commonly employed for the main structure. Therefore, the result relating to the transport properties (water permeability, chloride diffusivity) in this study should be useful to assess the durability of the structure made by a concrete that its composition is close to C_1 and C_2. Moreover, the proposed hydromechanical lattice model, fairly well validated against test result, can be used to predict the transport properties under a service loading for a specific concrete if its composition and its basic hydromechanical properties are known.

Declaration of Competing Interest

The authors declare that they have no known competing financial interests or personal relationships that could have appeared to influence the work reported in this paper.

Acknowledgement

This work is financially supported by the Ministry of Education and Training of Vietnam.

References

[1] AASHTO T277-86, (1990). "Rapid determination of the chloride permeability of concrete, Standard Specifications Part II, Tests", American Association of States Highway and Transportation Officials, Washington, D.C.

[2] AASHTO 259-80, (1990). "Resistance of concrete to chloride ion penetration, Standard Specifications Part II, Tests." American Association of States Highway and Transportation Officials, Washington, D.C.
[3] Y. Abbas, F. Pargar, D.A. Koleva, K. van Breugel, W. Olthuis, A. van den Berg, Non-destructive measurement of chloride ions concentration in concrete–a comparative analysis of limitations and prospects, Constr. Build. Mater. 174 (2018) 376–387.
[4] S.D. Abyaneh, H.S. Wong, N.R. Buenfeld, Simulating the effect of microcracks on the diffusivity and permeability of concrete using a three-dimensional model, Comput. Mater. Sci. 119 (2016) 130–143.
[5] A. Amriou, M. Bencheikh, New experimental method for evaluating the water permeability of concrete by a lateral flow procedure on a hollow cylindrical test piece, Constr. Build. Mater. 151 (2017) 642–649.
[6] ASTM C33, (2013). "Standard Specification for Concrete Aggregates." American Society for Testing and Materials.
[7] ASTM C150/C150M-18, (2018). "Standard Specification for Portland Cement." American Society for Testing and Materials.
[8] ASTM C1202-19, (2019). "Standard Test Method for Electrical Indication of Concrete's Ability to Resist Chloride Ion Penetration." American Society for Testing and Materials.
[9] ASTM C1556, (2016). "Standard Test Method for Determining the Apparent Chloride Diffusion Coefficient of Cementitious Mixtures by Bulk Diffusion." American Society for Testing and Materials.
[10] ASTM C136, (2014). "Standard Test Method for Sieve Analysis of Fine and Coarse Aggregates." American Society for Testing and Materials.
[11] ASTM C469, (2014). "Standard Test Method for Static Modulus of Elasticity and Poisson's Ratio of Concrete in Compression." American Society for Testing and Materials.
[12] ASTM C496, (2017). "Standard Test Method for Splitting Tensile Strength of Cylindrical Concrete Specimens." American Society for Testing and Materials.
[13] ASTM C39, (2017). "Standard Test Method for Compressive Strength of Cylindrical Concrete Specimens." American Society for Testing and Materials.
[14] F. Aurenhammer, Voronoi diagrams - a survey of fundamental geometric data structure, ACM Comput. Surv. 23 (1991) 345–405.
[15] N. Banthia, A. Birpava, S. Mindess, Permeability of concrete under stress, Cem. Concr. Res. 35 (2005) 1651–1655.
[16] M. Ben Romdhane, F. Ulm, Computational mechanics of the steel–concrete interface, Int. J. Numer. Anal. Meth. Geomech. 26 (2) (2002) 99–120.
[17] A. Bhargava, N. Banthia, Permeability of concrete with fiber reinforcement and service life predictions, Mater. Struct. 41 (2008) 363–372.
[18] A. Bhargava, N. Banthia, Measurement of concrete permeability under stress, Experimental Tech. 30 (5) (2006) 28–31.
[19] N.S. Berke, M.C. Hicks, Estimating the life cycle of reinforced concrete decks and marine piles using laboratory diffusion and corrosion data, in: V. Chaker (Ed.), Corrosion Forms and Control for Infrastructure, ASTM STP 1137, ASTM International, Philadelphia, Pennsylvania, 1992, pp. 207–231.
[20] J.E. Bolander, N. Sukumar, Irregular lattice model for quasi static crack propagation, Phys. Rev. B 71 (9) (2005) 094106.
[21] J.E. Bolander, S. Berton, Simulation of shrinkage induced cracking in cement composite overlays, Cem. Concr. Compos. 26 (2004) 861–871.
[22] J.E. Bolander, S. Saito, Fracture analysis using spring networks with random geometry, Eng. Fract. Mech. 61 (1998) 569–591.
[23] A. Caggiano, G. Etse, Coupled thermo–mechanical interface model for concrete failure analysis under high temperature, Comput. Methods Appl. Mech. Eng. 289 (2015) 498–516.
[24] S. Caré, E. Hervé, Application of a n-phase model to the diffusion coefficient of chloride in mortar, Transp. Porous Media 56 (2) (2004) 119–135.
[25] G. Chatzigeorgiou, V. Picandet, A. Khelidj, G. Pijaudier-Cabot, Coupling between progressive damage and permeability of concrete: analysis with a discrete model, Int. J. Numer. Anal. Meth. Geomech. 29 (10) (2005) 1005–1018.
[26] A. Daoud, O. Maurel, C. Laborderie, 2D mesoscopic modelling of bar–concrete bond, Eng. Struct. 49 (2013) 696–706.
[27] A. Delagrave, J.P. Bigas, J.P. Ollivier, J. Marchand, M. Pigeon, Influence of the interfacial zone on the chloride diffusivity of mortars, Adv. Cem. Based Mater. 5 (3–4) (1997) 86–92.
[28] A. Djerbi, S. Bonnet, A. Khelidj, V. Baroghel-Bouny, Effect of uniaxial compressive loading on gas permeability and chloride diffusion coefficient of concrete and their relationship, Cem. Concr. Res. 52 (2013) 131–139.
[29] A. Djerbi, S. Bonnet, A. Khelidj, V. Baroghel-Bouny, Influence of traversing crack on chloride diffusion into concrete, Cem. Concr. Res. 38 (2008) 877–883.
[30] J. Garboczi, Permeability, diffusivity and microstructural parameters: a critical review, Cem. Concr. Res. 20 (4) (1990) 590–601.
[31] P. Grassl, A lattice approach to model flow in cracked concrete, Cem. Concr. Compos. 31 (2009) 454–460.
[32] P. Grassl, Z.P. Bažant, Random lattice-particle simulation of statistical size effect in quasi-brittle structures failing at crack initiation, J. Eng. Mech. 135 (2) (2009) 85–92.
[33] P. Grassl, C. Fahy, D. Gallipoli, S.J. Wheeler, On a 2D hydro-mechanical lattice approach for modelling hydraulic fracture, J. Mech. Phys. Solids 75 (2015) 104–118.
[34] P. Grassl, D. Grégoire, L.R. Solano, G. Pijaudier-Cabot, Meso-scale modelling of the size effect on the fracture process zone of concrete, Int. J. Solids Struct. 49 (2012) 1818–1827.
[35] P. Grassl, H.S. Wong, N.R. Buenfeld, Influence of aggregate size and volume fraction on shrinkage induced micro-cracking of concrete and mortar, Cem. Concr. Res. 40 (2010) 85–93.
[36] P. Grassl, M. Jirásek, Meso-scale approach to modelling the fracture process zone of concrete subjected to uniaxial tension, Int. J. Solids Struct. 47 (2010) 957–968.
[37] P. Grassl, C. Pearce, Mesoscale approach to modeling concrete subjected to thermomechanical loading, J. Eng. Mech. 136 (3) (2010) 322–328.
[38] C.P. Gu, G. Ye, W. Sun, A review of the chloride transport properties of cracked concrete: experiments and simulations, J. Zhejiang Univ.-Sci. A (Applied Physics & Engineering) 16 (2) (2015) 81–92.
[39] M. Hoseini, V. Bindiganavile, N. Banthia, The effect of mechanical stress on permeability of concrete: a review, Cem. Concr. Compos. 31 (4) (2009) 213–220.
[40] A. Kermani, Permeability of stressed concrete, Build. Res. Inf. 19 (6) (1991) 360–366.
[41] S.M. Kim, R.K. Abu Al-Rub, Mesoscale computational modeling of the plastic damage response of cementitious composites, Cem. Concr. Res. 41 (3) (2011) 339–358.
[42] M. Ismail, A. Toumi, R. Francois, R. Gagne, Effect of crack opening on the local diffusion of chloride in cracked mortar samples, Cem. Concr. Res. 38 (8–9) (2008) 1106–1111.
[43] M. Ismail, A. Toumi, R. Francois, R. Gagne, Effect of crack opening on the local diffusion of chloride in inert materials, Cem. Concr. Res. 34 (2004) 711–716.
[44] C.A. Jones, Z.C. Grasley, Correlation of radial flow-through and hollow cylinder dynamic pressurization test for measuring permeability, J. Mater. Civil Eng. 21 (10) (2009) 594–600.
[45] X.X. Li, Q. Xu, S.H. Chen, An experimental and numerical study on water permeability of concrete, Constr. Build. Mater. 105 (2016) 503–510.
[46] A. Michou, A. Hilaire, F. Benboudjema, G. Nahas, P. Wyniecki, Y. Berthaud, Reinforcement–concrete bond behavior: experimentation in drying conditions and meso-scale modeling, Eng. Struct. 101 (2015) 570–582.
[47] J.L. Marriaga, P. Claisse, Effect of the non-linear membrane potential on the migration of ionic species in concrete, Electrochim. Acta 54 (2009) 2761–2769.
[48] NT BUILD 492, (1999). "Concrete, mortar, and cement-based repair materials: chloride migration coefficient from non-steady state migration experiments." Nordtest, Espoo, Finland, 1999.
[49] NT BUILD 443, (1995). "Concrete, hardened: Accelerated chloride penetration." Nordtest, Espoo, Finland.
[50] S.T. Nguyen, D.C. Pham, M.N. Vu, Q.D. To, On the effective transport properties of heterogeneous materials, Int. J. Eng. Sci. 104 (2016) 75–86.
[51] T.D. Nguyen, D.T. Pham, M.N. Vu, Thermo-mechanically-induced thermal conductivity change and its effect on the behaviour of concrete, Constr. Build. Mater. 198 (2019) 98–105.
[52] B.H. Oh, S.Y. Jang, Effects of material and environmental parameters on chloride penetration profiles in concrete structures, Cem. Concr. Res. 37 (2007) 47–53.
[53] A. Okabe, B. Boots, K. Sugihara, S.N. Chiu, Spatial Tessellations, Wiley, New York, 2000.
[54] B. Patzák, Object oriented finite element modeling, Acta Polytech. 39 (1999) 99–113.
[55] Q.T. Phung, M. Norbert, S. Geert De, J. Diederik, Y. Guang, Determination of water permeability of cementitious materials using a controlled constant flow method, Constr. Build. Mater. 47 (2013) 1888–1896.
[56] E. Poulsen, L. Mejlbro, Diffusion of Chloride in Concrete: Theory and Application, Taylor & Francis, New York (USA), 2006.
[57] A. Pouya, M.N. Vu, S. Ghabezloo, Z. Bendjeddou, Effective permeability of cracked unsaturated porous materials, Int. J. Solids Struct. 50 (20–21) (2013) 3297–3307.
[58] B. Šavija, J. Pacheco, E. Schlangen, Lattice modeling of rapid chloride migration in concrete, Cem. Concr. Res. 61–62 (2014) 49–63.
[59] B. Šavija, J. Pacheco, E. Schlangen, Lattice modeling of chloride diffusion in sound and cracked. concrete, Cem. Concr. Compos. 42 (2013) 30–40.
[60] M. Sahmaran, Effect of flexure induced transverse crack and self-healing on chloride diffusivity of reinforced mortar, J. Mater. Sci. 42 (2007) 9131–9136.
[61] K.L. Scrivener, A.K. Crumbie, P. Laugesen, The interfacial transition zone (ITZ) between cement paste and aggregate in concrete, Interface Sci. 12 (4) (2004) 411–421.
[62] L. Shen, Q. Ren, N. Xia, L. Sun, X. Xia, Mesoscopic numerical simulation of effective thermal conductivity of tensile cracked concrete, Constr. Build. Mater. 95 (2015) 467–475.
[63] M. Souley, F. Homand, S. Pepa, D. Hoxha, Damage-induced permeability changes in granite: a case example at the URL in Canada, Int. J. Rock Mech. Min. Sci. 38 (2) (2001) 297–310.
[64] M. Torres-Luque, E. Bastidas-Arteaga, F. Schoefs, M. Sánchez-Silva, J.F. Osma, Non-destructive methods for measuring chloride ingress into concrete: stateof-the-art and future challenges, Constr. Build. Mater. 68 (2014) 68–81.
[65] R. Van Noort, M. Hunger, P. Spiesz, Long-term chloride migration coefficient in slag cement-based concrete and resistivity as an alternative test method, Constr. Build. Mater. 115 (2016) 746–759.
[66] M.N. Vu, A. Pouya, D. Seyedi, Effective permeability of three-dimensional porous media containing anisotropic distributions of oriented elliptical disc-shaped fractures with uniform aperture, Adv. Water Resour. 118 (2018) 1–11.
[67] M.N. Vu, S.T. Nguyen, Q.D. To, N.H. Dao, Theoretical predicting of permeability evolution in damaged rock under compressive stress, Geophys. J. Int. 209 (2) (2017) 1352–1361.
[68] Y. Wang, K. Fu, Comparisons of instantaneous chloride diffusion coefficients determined by RCM method and chloride natural diffusion test, Constr. Build. Mater. 223 (2019) 595–604.

[69] J. Wang, P.A.M. Basheer, S.V. Nanukuttan, A.E. Long, Y. Bai, Influence of service loading and the resulting micro-cracks on chloride resistance of concrete, Constr. Build. Mater. 108 (2016) 56–66.
[70] L.C. Wang, T. Ueda, Mesoscale modelling of the chloride diffusion in cracks and cracked concrete, J. Adv. Concr. Technol. 9 (3) (2011) 241–249.
[71] L.C. Wang, T. Ueda, Mesoscale modeling of water penetration into concrete by capillary absorption, Ocean Eng. 38 (2011) 519–528.
[72] P.P. Win, M. Watanabe, A. Machida, Penetration profile of chloride ion in cracked reinforced concrete, Cem. Concr. Res. 34 (2004) 1073–1079.
[73] Q. Yuan, C. Shi, G. De Schutter, K. Audenaert, D. Deng, Chloride binding of cement-based materials subjected to external chloride environment–a review, Constr. Build. Mater. 23 (2009) 1–13.
[74] C.S. Zhou, K.F. Li, Numerical and statistical analysis of permeability of concrete as a random heterogeneous composite, Comput. Concr. 7 (5) (2010) 469–482.
[75] C.L. Zhang, The stress-strain-permeability behaviour of clay rock during damage and recompaction, J. Rock Mech. Geotech. Eng. 8 (1) (2016) 16–26.